

Article

The Effects of Excess Co on the Phase Composition and Thermoelectric Properties of Half-Heusler NbCoSb

Lihong Huang ¹ , Junchen Wang ¹, Xi Chen ¹, Ran He ², Jing Shuai ³, Jianjun Zhang ^{1,*}, Qinyong Zhang ¹ and Zhifeng Ren ^{3,*}

¹ Key Laboratory of Fluid and Power Machinery of Ministry of Education, School of Materials Science & Engineering, Xihua University, Chengdu 610039, China; huang.lihong@foxmail.com (L.H.); junchenwang123@sina.com (J.W.); 15183544928@163.com (X.C.); bohr123@163.com (Q.Z.)

² Institute for Metallic Materials, IFW-Dresden, 01069 Dresden, Germany; zhizhishangshan@gmail.com

³ Department of Physics and TcSUH, University of Houston, Houston, TX 77204, USA; jshuai@uh.edu

* Correspondence: zjjxjtu@163.com (J.Z.); zren@uh.edu (Z.R.); Tel.: +86-028-8772-9250 (J.Z.)

Received: 12 April 2018; Accepted: 9 May 2018; Published: 11 May 2018



Abstract: NbCoSb with nominal 19 valence electrons, and is supposed to be metallic, has recently been reported to also exhibit the thermoelectric properties of a heavily doped n-type semiconductor. In this study, we prepared Co-rich NbCo_{1+x}Sb samples ($x = 0, 0.2, 0.3, 0.4, 0.5$), and their phase compositions, microstructures and thermoelectric properties were investigated. The Seebeck coefficient increased a great deal with increasing x , due to decreasing carrier concentration, and the total thermal conductivity reduced mainly because of declining κ_e . Finally, a peak thermoelectric figure of merit, ZT , was about 0.46 for NbCo_{1.3}Sb at 973 K. This enhancement was mainly attributed to the reduction of electric thermal conductivity and the increase of Seebeck coefficient. The excess Co had effects on the carrier concentration, deformation potential E_{def} and DOS effective mass m^* . Adding an excessive amount of Co leads to a very high E_{def} , which was detrimental for transport characteristics.

Keywords: half-Heusler; NbCoSb; excess Co; thermoelectric performance

1. Introduction

Thermoelectric (TE) materials can directly convert waste heat into electricity in an environmentally-friendly way and have received a great deal of attention owing to global energy sources and environmental challenges [1]. The conversion efficiency of a TE material is determined by the dimensionless figure of merit $ZT = S^2\sigma T/(\kappa_e + \kappa_L)$, where S , σ , T , κ_e , and κ_L are the Seebeck coefficient, electrical conductivity, absolute temperature, and electronic and lattice components of the thermal conductivity, respectively. It is hard to achieve a high ZT by simply improving one of these parameters, because S , σ , κ_e are strongly coupled with each other [2]. Hence, the optimization of carrier concentrations is an essential requirement [3].

Usually, an ideal thermoelectric material should have a glass-like heat conduction of phonons and crystal-like electrical conduction of charge carriers. This strategy is referred to as “phonon-glass electron-crystal”, and was first introduced by Slack [4]. To improve phonon transport properties, various approaches have been used to enhance phonon scattering and decrease κ_L , such as introducing secondary phase [5], nanoscale crystalline grain [6] and point defect [7]. To enhance electron transport properties, a series of band structure engineering approaches have been developed to tune the power factor ($S^2\sigma$) by optimizing carrier concentration [8] or energy resonant doping [9].

Recently, particular attention has been paid to half-Heusler (HH) compounds, due to their high-temperature stability, good mechanical robustness, and good TE performance, which are of

paramount importance for practical applications. Typical semiconducting HH compounds with 18 valence electrons per unit cell, ZrCoSb, ZrNiSn, TiNiSn, NbFeSb, and their alloys have been intensively investigated as promising medium–high temperature TE materials [10–16]. Additionally, an exciting ZT of about 1.5 at 1200 K has been realized in p-type NbFeSb alloys [17,18]. Surprisingly, our previous work showed that NbCoSb with nominal 19 valence electrons, which is supposed to be metallic, exhibited fairly good n-type TE performance and achieved a peak ZT of ~ 0.4 at 973 K [19]. The experimental results indicated that NbCoSb is a heavily doped n-type semiconductor with high carrier concentration.

From our previous work, we know that NbCoSb has a comparatively low Seebeck coefficient and a higher thermal conductivity. According to Chai's report [20,21], ZT of ZrNi_{1.1}Sn was approx. 40% higher compared to ZrNiSn, due to the secondary phase in the matrix introduced by excess Ni. It provided a great basis for phonon-scattering centers, leading to an improved Seebeck coefficient and a reduced thermal conductivity [20,21]. Inspired by this feature, this work aimed at qualitatively investigating the effects of excess Co on the microstructures and thermoelectric properties of HH alloy NbCoSb. The Co-rich samples with nominal compositions of NbCo_{1+x}Sb ($x = 0, 0.2, 0.3, 0.4, 0.5$) were prepared through arc melting, following by ball milling and hot pressing. The evaluation and comparison of phase composition and TE properties of NbCo_{1+x}Sb were performed. Additionally, the electrical transport characteristics of Co-rich NbCoSb materials were also analyzed using the single parabolic band (SPB) model.

2. Experimental Procedures

A series of Co-rich NbCoSb samples were prepared by arc melting followed by ball milling and hot pressing. High purity niobium slugs (Nb, 99.99%, Alfa Aesar, Ward Hill, MA, USA), cobalt pieces (Co, 99.95%, Alfa Aesar), and antimony rods (Sb, 99.8%, Alfa Aesar) were weighed according to the composition of NbCo_{1+x}Sb ($x = 0, 0.2, 0.3, 0.4, 0.5$). For all samples, 5 at% more Sb was added in order to compensate the loss of Sb during arc melting. In order to get homogeneous ingots, metallic raw materials were arc-melted five times reversely under argon protection. The obtained ingots were ball milled (SPEX 8000M Mixer/Mill, Metuchen, NJ, USA) for 7 hours under argon protection. Thereafter, the ball-milled powders were loaded into a graphite die and sintered by direct current-induced hot pressing at 1273 K for 2 min under 77 MPa to get pellet samples. The thickness of the as-hot-pressed samples was about 2 mm.

The thermal conductivity $\kappa = dDC_p$ was calculated using the measured density (d) by Archimedes method, thermal diffusivity (D) by laser flash method (LFA 457, Netzsch), and specific heat capacity (C_p) by differential scanning calorimetry (DSC 404 C, Netzsch, Selb, Germany). Bar-shaped samples of about 2 mm \times 2 mm \times 10 mm were used for measuring the electrical conductivity and Seebeck coefficient simultaneously from 300 to 973 K (ZEM-3, ULVAC Riko, Chigasaki, Japan). The Hall coefficient (R_H) was measured at room temperature by a commercial system (PPMS D060, Quantum Design, San Diego, CA, USA) using a four-probe configuration and the Van der Pauw method, with a magnetic field of 3.0 T and an electrical current of 8 mA. The carrier concentration (n) was calculated by $n = 1/(eR_H)$, and the carrier mobility (μ) was estimated by $\sigma = ne\mu$. The properties of the samples were isotropic, due to their small grain size and random crystal orientation.

The phase structure of the samples was observed using XRD on a PANalytical X'Pert Pro diffractometer (Malvern Panalytical, Almelo, Holland) and Cu K α radiation. The fresh section of the hot-pressed sample NbCo_{1.3}Sb was studied via SEM (JEOL 6330F, Deerbrook, WI, USA) to show the particle size.

3. Results and Discussion

Figure 1a shows the XRD patterns of hot-pressed bulk samples NbCo_{1+x}Sb ($x = 0, 0.2, 0.3, 0.4, 0.5$) which can be classified as cubic MgAgAs-type crystal structure (JCPDS 51-1247, $a = 0.5897$ nm). The dominant phase of all samples was the half-Heusler phase of NbCoSb, while a small number of

secondary phases such as Nb_3Sb , $\text{Nb}_{1.08}\text{Co}_{1.92}$, and NbCo_2 were observed following the increasing content of excess Co, respectively. Based on the binary phase diagram of Nb and Sb, Nb_3Sb may be formed, due to the peritectic reaction during the cooling process ($x = 0$), as shown in Figure 1b. With a small amount of excess Co ($x = 0.2, 0.3$), the secondary phases Nb_3Sb disappeared. However, another secondary phase $\text{Nb}_{1.08}\text{Co}_{1.92}$ was introduced in a small amount. A new secondary phase NbCo_2 was observed for the Co-rich sample $\text{NbCo}_{1.4}\text{Sb}$, with increased content of excess Co. Even more NbCo_2 appeared for $\text{NbCo}_{1.5}\text{Sb}$. These phenomena indicate a scale of Co solubility in the structure. However, when x exceeded 0.3, it precipitated out the other second phase of NbCo_2 .

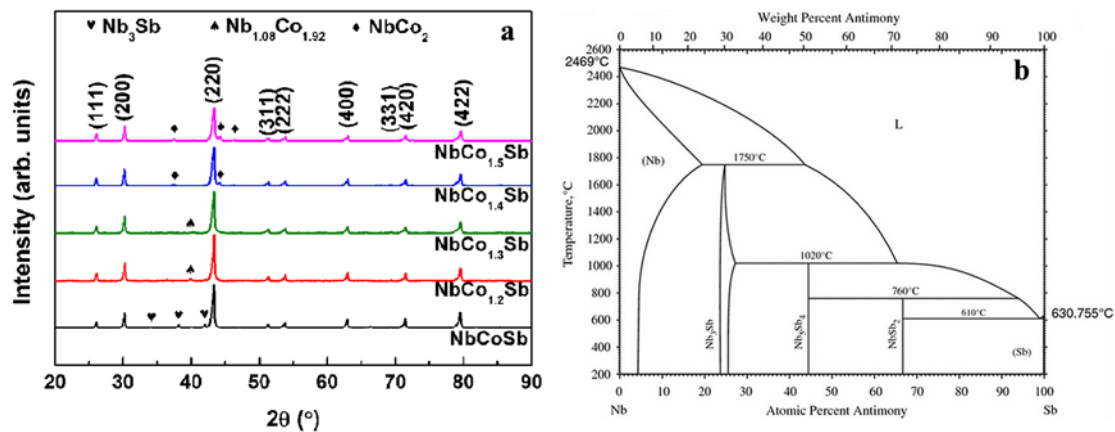


Figure 1. XRD patterns of bulk $\text{NbCo}_{1+x}\text{Sb}$ ($x = 0, 0.2, 0.3, 0.4, 0.5$) samples (a) the binary phase diagram of Nb and Sb (b).

Table 1 shows the lattice parameter, theoretical, experimental, and relative density of $\text{NbCo}_{1+x}\text{Sb}$ samples. The lattice parameter increased with increasing x , mainly due to the solid solution of excess Co, leading to lattice expansion of HH phase. The theoretical density was calculated by $d_{\text{cal}} = \sum n_i M_i / (a^3 N_A)$, where n_i is the number of atoms of Nb, Co and Sb per unit cell, M_i the corresponding atomic mass of each element, a the lattice parameter, and N_A the Avogadro constant ($6.023 \times 10^{23} \text{ mol}^{-1}$). The relative density was more than 90% for $x = 0, 0.2, 0.3$ and approx. 85–86% for $x = 0.4$ and 0.5. The low relative density of the $\text{NbCo}_{1.4}\text{Sb}$ and $\text{NbCo}_{1.5}\text{Sb}$ samples may be due to inaccurate estimation of the theoretical density. The additional Co did not fully enter the lattice, but form the second phase, while we ignored this in our calculations.

Table 1. Lattice parameter, theoretical, experimental, and relative density of $\text{NbCo}_{1+x}\text{Sb}$ ($x = 0, 0.2, 0.3, 0.4, 0.5$) samples.

Nominal Composition	Lattice Parameter (nm)	Density (g cm^{-3})		Relative Density (%)
		Theoretical	Experimental	
NbCoSb	0.5890	8.893	8.329	93.66
$\text{NbCo}_{1.2}\text{Sb}$	0.5893	9.262	8.345	90.10
$\text{NbCo}_{1.3}\text{Sb}$	0.5895	9.443	8.637	91.46
$\text{NbCo}_{1.4}\text{Sb}$	0.5896	9.634	8.310	86.26
$\text{NbCo}_{1.5}\text{Sb}$	0.5897	9.817	8.342	84.98

As shown in Figure 2, there were no pores in our hot-pressed sample $\text{NbCo}_{1.3}\text{Sb}$, indicating a high relative density. Moreover, the grain size of the sample was approx. several hundreds of nanometers.

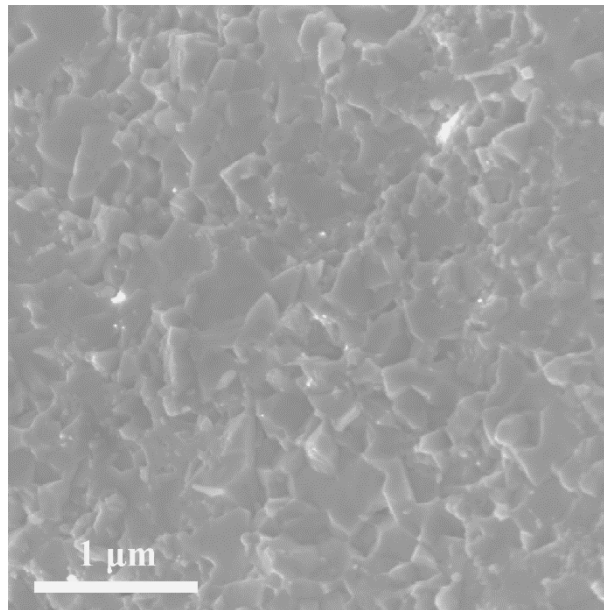


Figure 2. SEM image of hot pressed sample NbCo_{1.3}Sb.

Figure 3 shows the electrical properties as a function of temperature for NbCo_{1+x}Sb. The electrical conductivity of NbCo_{1+x}Sb decreased with increasing temperature for $x = 0, 0.2, 0.3$, indicating the characteristics of metal (Figure 3a). However, the trend of decreasing electrical conductivity with increasing temperature was not determinable for NbCo_{1.4}Sb and NbCo_{1.5}Sb. Apparently, the additional Co reduced the electrical conductivity, and the decrease was not present for $x = 0.5$. For NbCo_{1.3}Sb, the electrical conductivity was approx. $1.83 \times 10^5 \text{ S m}^{-1}$ at room temperature and reached approx. $0.83 \times 10^5 \text{ S m}^{-1}$ at 973 K. As shown in Figure 3b, the negative Seebeck coefficients of all samples indicated a n-type conduction behavior. The Seebeck coefficient of NbCo_{1.3}Sb was approx. $-70 \mu\text{V K}^{-1}$ at room temperature and $\sim -154 \mu\text{V K}^{-1}$ at 973 K. The Seebeck coefficient enhanced gradually with increasing excess Co content, which could partly be explained by a decreasing Hall carrier concentration (Table 2). The power factor for NbCo_{1.3}Sb was $\sim 9 \times 10^{-4} \text{ W m}^{-1} \text{ K}^{-2}$ at room temperature and $\sim 20 \times 10^{-4} \text{ W m}^{-1} \text{ K}^{-2}$ at 973 K (Figure 3c). The power factor was maintained or decreased after adding excess Co, especially for NbCo_{1.4}Sb and NbCo_{1.5}Sb, due to their low electrical conductivity. Pisarenko plot of $|S|$ versus carrier concentration (n) at room temperature was calculated based on Equations (1)–(6) using a SPB model. The results are shown in Figure 3d [22,23].

$$S = \pm \frac{k_B}{e} \left(\frac{(r + 5/2)F_{r+3/2}(\eta)}{(r + 3/2)F_{r+1/2}(\eta)} - \eta \right) \quad (1)$$

$$F_n(\eta) = \int_0^\infty \frac{x^n}{1 + e^{x-\eta}} dx \quad (2)$$

$$L = \left(\frac{k_B}{e} \right)^2 \left[\frac{(r + 7/2)F_{r+5/2}(\eta)}{(r + 3/2)F_{r+1/2}(\eta)} - \left(\frac{(r + 5/2)F_{r+3/2}(\eta)}{(r + 3/2)F_{r+1/2}(\eta)} \right)^2 \right] \quad (3)$$

$$r_H = \frac{3}{2} F_{1/2}(\eta) \frac{(3/2 + 2r)F_{2r+1/2}(\eta)}{(3/2 + r)^2 F_{r+1/2}^2(\eta)} \quad (4)$$

$$n = \frac{4\pi(2m^*k_B T)^{3/2} F_{1/2}(\eta)}{h^3 r_H} \quad (5)$$

$$m^* = \frac{h^2}{2k_B T} \left[\frac{n \times r_H}{4\pi F_{1/2}(\eta)} \right]^{2/3} \quad (6)$$

where $F_n(\eta)$ is the n th order Fermi integral, η the reduced Fermi energy, e the electron charge, r the scattering factor, k_B the Boltzmann's constant, h the Plank's constant, r_H the Hall factor, and x the variable of integration. $r = -1/2$ was used for the acoustic phonon scattering mechanism. Combining the experimental carrier concentrations and Seebeck coefficients, a density of states (DOS) effective mass $m^* \sim 8.5 m_e$ was derived for Co-rich samples $\text{NbCo}_{1+x}\text{Sb}$. Therefore, the improvements of Seebeck coefficients for Co-rich samples could be explained by their relatively high DOS effective mass m^* and reduced carrier concentration.

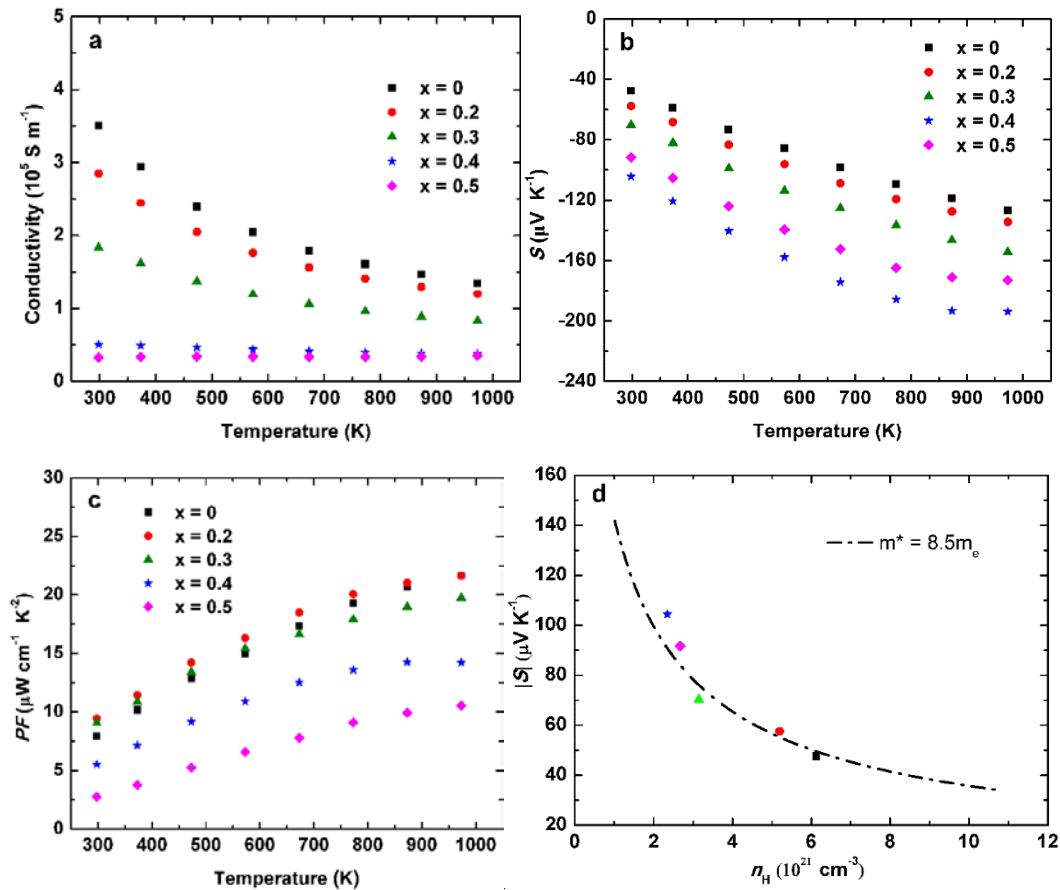


Figure 3. (a) Temperature-dependent electrical conductivity; (b) Seebeck coefficient; (c) power factor; and (d) Pisarenko plot for $\text{NbCo}_{1+x}\text{Sb}$.

Table 2. Hall coefficient, carrier concentration, Hall mobility, effective mass, and deformation potential of $\text{NbCo}_{1+x}\text{Sb}$ ($x = 0, 0.2, 0.3, 0.4, 0.5$) at room temperature.

Nominal Composition	R_H	n_H (10^{21} cm^{-3})	μ_H ($\text{cm}^2 \text{ V}^{-1} \text{ s}^{-1}$)	E_{def} (eV)
NbCoSb	−1.03	6.04	3.62	18.86
NbCo _{1.2} Sb	−1.21	5.16	3.45	18.21
NbCo _{1.3} Sb	−2.01	3.11	3.68	21.93
NbCo _{1.4} Sb	−2.66	2.35	1.34	30.71
NbCo _{1.5} Sb	−2.27	2.75	0.74	41.38

Table 2 shows the electrical transport properties of all samples at room temperature. Hall coefficients showed negative values, indicating n-type conduction with electrons as major carriers, which was consistent with the negative values of the Seebeck coefficients. Obviously, the carrier concentration decreased with increasing x . The mobility of the Co-rich samples was largely

decreased for $x = 0.4$ and 0.5 , which may be due to their enhanced effective mass and existence of secondary phases.

The deformation potential E_{def} specifically characterizes the scattering effects of lattice vibration on carriers, namely the coupling effects between phonons and electrons. E_{def} can be roughly estimated by Equation (7) when acoustic phonon scattering is dominant [24,25].

$$E_{def}^2 = \frac{F_0(\eta)}{2F_{1/2}(\eta)} \frac{2\sqrt{2}e\pi h^4}{3(k_B T)^{3/2}} \frac{dv_l^2 N_v^{5/3}}{\mu_H(m^*)^{5/2}} \quad (7)$$

where d is the density (approx. 8.8 g cm^{-3}), v_l the longitudinal velocity of sound (approx. 5488 m s^{-1}), μ_H the drift mobility ($\mu_H = \mu/r_H$), and Nv the number of degenerate carrier pockets. The deformation potential E_{def} of $\text{NbCo}_{1.5}\text{Sb}$ was found to be 41.38 eV (Table 2), a relatively large value, being detrimental for electrical transport properties. It was much higher than the one of $\text{NbCoSb}_{0.8}\text{Sn}_{0.2}$ (approx. 21 eV) [26].

Figure 4 shows the thermal transport properties of $\text{NbCo}_{1+x}\text{Sb}$. Obviously, diffusivity showed a negative linear relationship with temperature and slightly decreased after adding excess Co except for $x = 0.5$ (Figure 4a). As shown in Figure 4b, the total thermal conductivity κ of $\text{NbCo}_{1+x}\text{Sb}$ decreased with increasing x , primarily due to reduced electronic thermal conductivities. Besides, κ decreased during the whole test temperature range, because of the Umklapp scattering process, indicating no bipolar effect for this system. The total thermal conductivity is the sum of lattice thermal conductivity κ_L and electronic thermal conductivity κ_e , assuming negligible bipolar effect. The Wiedemann–Franz relation $\kappa_e = L\sigma T$ —where L is the Lorenz number which can be estimated using SPB model by acoustic phonon scattering using Equations (1)–(3)—combines the measured Seebeck coefficients. The calculated Lorenz constant was approx. $2.0 \times 10^{-8} \text{ W } \Omega \text{ K}^{-2}$ for $\text{NbCo}_{1.3}\text{Sb}$ at room temperature. κ_L could be calculated by subtraction of κ_e from κ . As shown in Figure 4c,d, κ_L increased slightly for Co-rich samples, while κ_e dropped steadily over the whole measured temperature range. Here, the reduction of κ_e can be primarily ascribed to both the reduction of L and σ . The obvious decrease of κ_e happened due to reduced carrier concentration, contributing to a reduced Lorenz constant. Typically, κ_e at room temperature decreased more than 70% from $2.34 \text{ W m}^{-1} \text{ K}^{-1}$ for NbCoSb to $0.19 \text{ W m}^{-1} \text{ K}^{-1}$ for $\text{NbCo}_{1.5}\text{Sb}$. Moreover, the slight increase of κ_L may be due to weakened electron-phonon scattering, which became weaker for Co-rich samples [27]. It might also related to the existence of impurity phases $\text{Nb}_{1.08}\text{Co}_{1.92}$ and NbCo_2 , or other possible phonon scattering.

Furthermore, we estimated the minimum lattice thermal conductivity (κ_{min}) of NbCoSb using Cahill’s method, assuming the phonon’s mean free path is half of the phonon’s wavelength [28]:

$$\kappa_{min} = \frac{1}{2} \left(\frac{\pi}{6} \right)^{1/3} k_B V^{-2/3} (2v_t + v_l) \quad (8)$$

where V , v_t , and v_l are average volume per atom, transversal and longitudinal wave velocity (both measured at room temperature; $v_t = 3059 \text{ m s}^{-1}$, $v_l = 5488 \text{ m s}^{-1}$), respectively. In general, κ was found to be larger than the estimated $\kappa_{min} \approx 0.9 \text{ W m}^{-1} \text{ K}^{-1}$. It seems that there is a large potential to improve the ZT values by further reducing the lattice thermal conductivity of NbCoSb based TE materials, definitely, further efforts are required to explore new useful ways to enhance the thermoelectric performance.

Combining all transport properties, the figure of merit ZT was calculated as a function of temperature as shown in Figure 5. The peak ZT of 0.46 was obtained at 973 K for sample $\text{NbCo}_{1.3}\text{Sb}$. A slight increase of ZT should contribute to decreased thermal conductivity and a moderate PF .

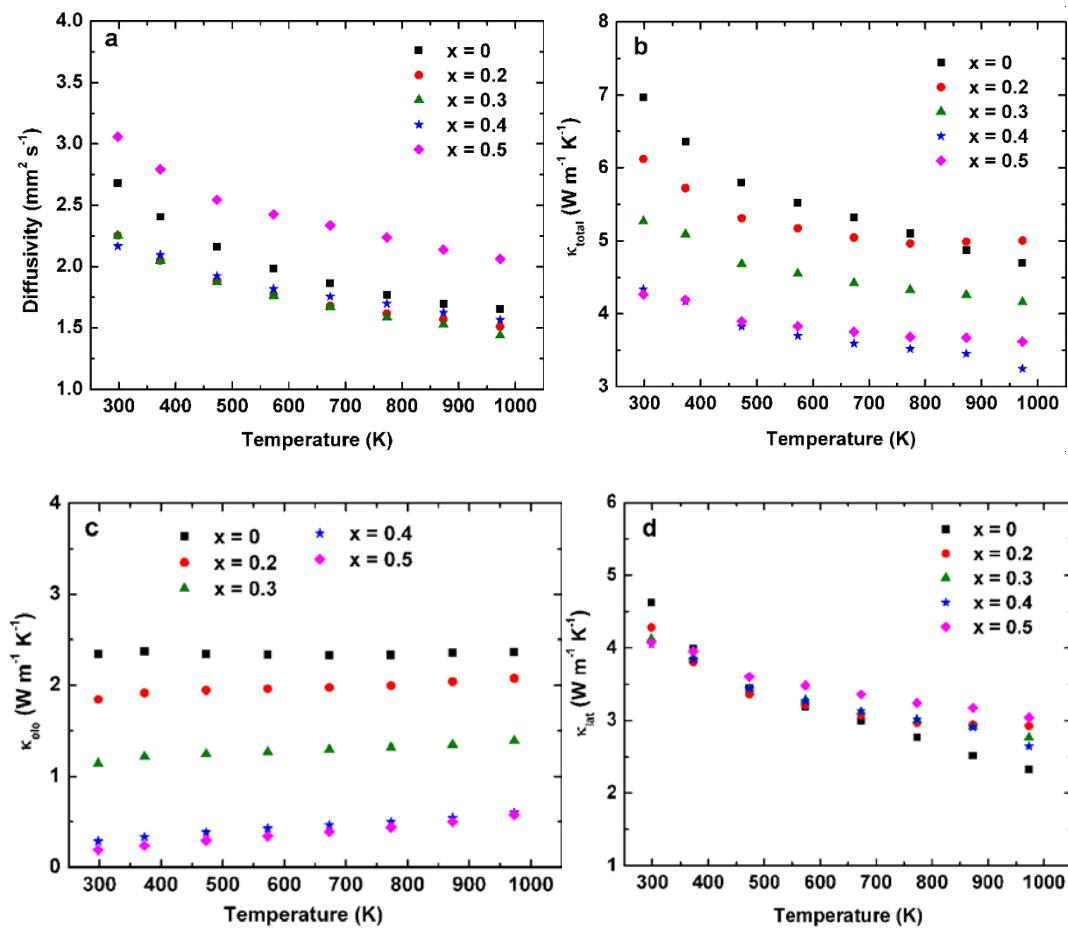


Figure 4. (a) Temperature-dependent thermal diffusivity; (b) total thermal conductivity; (c) electronic thermal conductivity; and (d) lattice thermal conductivity for NbCo_{1+x}Sb.

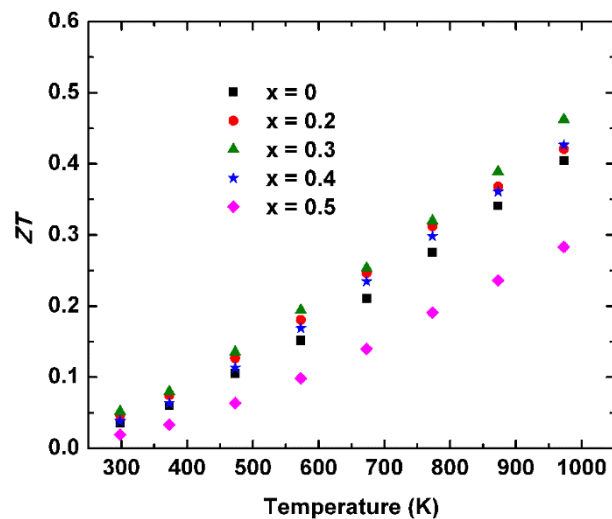


Figure 5. Temperature dependent ZT values of half-Heusler compounds NbCo_{1+x}Sb (x = 0, 0.2, 0.3, 0.4, 0.5).

4. Conclusions

In summary, Co-rich samples NbCo_{1+x}Sb (x = 0, 0.2, 0.3, 0.4, 0.5) were synthesized and characterized. A small change in lattice parameter indicated a certain degree of Co solution into

half-Heusler matrix. Adding excess Co eliminated the secondary phase of Nb₃Sb, while other impurity phases such as Nb_{1.08}Co_{1.92} and NbCo₂ appeared with more excess Co. With increasing x , the Seebeck coefficient increased a lot due to decreasing carrier concentration; total thermal conductivity decreased mainly because of declining κ_e . Adding an excessive amount of Co leads to a very high deformation potential E_{def} , such as NbCo_{1.5}Sb (41.38 eV), which is detrimental for transport characteristics. Finally, a maximum ZT value of approx. 0.46 for NbCo_{1.3}Sb was obtained at 973 K.

Author Contributions: Conceptualization, L.H. and J.Z.; Methodology, L.H.; Software, L.H.; Validation, L.H. and Z.R.; Formal Analysis, L.H., Q.Z.; Investigation, J.W.; Resources, R.H. and J.Z.; Data Curation, X.C.; Writing-Original Draft Preparation, L.H.; Writing-Review & Editing, L.H.; Supervision, L.H. and Z.R.; Project Administration, J.S. and Z.R.

Funding: The work performed at Xihua University was funded by the Young Scientist Fund of National Natural Science Foundation of China (No. 51601152), the Open Research Subject of Key Laboratory of Fluid and Power Machinery (Xihua University), Ministry of Education (No. SZJJ2017-082), the Open Research Subject of Key Laboratory of Special Materials and Manufacturing Technology (No. SZJJ2016-034), the Chunhui Program from Education Ministry of China (No. Z2015094, No. Z2015082), National Natural Science Foundation of China (No. 51372208, No. 51472207, No. 51572226), and that at the University of Houston is supported by “Solid State Solar Thermal Energy Conversion Center (S³TEC)”, an Energy Frontier Research Center funded by the U.S. Department of Energy, Office of Science, Office of Basic Energy Science under award number DE-SC0001299.

Conflicts of Interest: The authors declare no conflict of interest.

References

- Mao, J.; Wu, Y.X.; Song, S.W.; Shuai, J.; Liu, Z.H.; Pei, Y.Z.; Ren, Z.F. Anomalous electrical conductivity of n-type Te-doped Mg_{3.2}Sb_{1.5}Bi_{0.5}. *Mater. Today Phys.* **2017**, *3*, 1–6. [[CrossRef](#)]
- Ioffe, A.F. *Semiconductor Thermoelements and Thermoelectric Cooling*; Infosearch: London, UK, 1957.
- Goldsmid, H.J. *Thermoelectric Refrigeration*; Plenum Press: New York, NY, USA, 1964.
- Lin, S.Q.; Li, W.; Li, S.S.; Zhang, X.Y.; Chen, Z.W.; Xu, Y.D.; Chen, Y.; Pei, Y.Z. High thermoelectric performance of Ag₉GaSe₆ enabled by low cutoff frequency of acoustic phonons. *Joule* **2017**, *1*, 816–830. [[CrossRef](#)]
- Wu, Y.X.; Li, W.; Faghaninia, A.; Chen, Z.W.; Li, J.; Zhang, X.Y.; Gao, B.; Lin, S.Q.; Zhou, B.Q.; Jain, A.; et al. Promising thermoelectric performance in van der Waals layered SnSe₂. *Mater. Today Phys.* **2017**, *3*, 127–136. [[CrossRef](#)]
- Rogl, G.; Rogl, P. How nanoparticles can change the figure of merit, ZT , and mechanical properties of skutterudites. *Mater. Today Phys.* **2017**, *3*, 48–69. [[CrossRef](#)]
- Zhang, Q.; Chere, E.K.; McEnaney, K.; Yao, M.L.; Cao, F.; Ni, Y.Z.; Chen, S.; Opeil, C.; Chen, G.; Ren, Z.F. Enhancement of thermoelectric performance of n-type PbSe by Cr doping with optimized carrier concentration. *Adv. Energy Mater.* **2015**, *5*, 1401977. [[CrossRef](#)]
- Berry, T.; Fu, C.G.; Auffermann, G.; Fecher, G.H.; Schnelle, W.; Sanchez, F.S.; Yue, Y.; Liang, H.; Felser, C. Enhancing thermoelectric performance of TiNiSn half-Heusler compounds via modulation doping. *Chem. Mater.* **2017**, *29*, 7042–7048. [[CrossRef](#)]
- Chen, L.; Liu, Y.M.; He, J.; Tritt, T.M.; Poon, S.J. High thermoelectric figure of merit by resonant dopant in half-Heusler alloys. *AIP Adv.* **2017**, *7*, 065208. [[CrossRef](#)]
- Silpawilawan, W.; Kurosaki, K.; Ohishi, Y.; Muta, H.; Yamanaka, S. FeNbSb p-type half-Heusler compound: beneficial thermomechanical properties and high-temperature stability for thermoelectrics. *J. Mater. Chem. C* **2017**, *5*, 6677–6681. [[CrossRef](#)]
- Zeier, W.G.; Anand, S.; Huang, L.H.; He, R.; Zhang, H.; Ren, Z.F.; Wolverton, C.; Snyder, G.J. Using the 18-electron rule to understand the nominal 19-electron half-Heusler NbCoSb with Nb vacancies. *Chem. Mater.* **2017**, *29*, 1210–1217. [[CrossRef](#)]
- He, R.; Zhu, H.T.; Sun, J.Y.; Mao, J.; Reith, H.; Schierning, S.C.G.; Nielsch, K.; Ren, Z.F. Improved thermoelectric performance of n-type half-Heusler MCo_{1-x}Ni_xSb (M = Hf, Zr). *Mater. Today Phys.* **2017**, *1*, 24–30. [[CrossRef](#)]
- Zhang, H.; Wang, Y.M.; Huang, L.H.; Chen, S.; Dahal, H.; Wang, D.Z.; Ren, Z.F. Synthesis and thermoelectric properties of n-type half-Heusler compound VCoSb with valence electron count of 19. *J. Alloys Compd.* **2016**, *654*, 321–326. [[CrossRef](#)]

14. Huang, L.H.; Wang, Y.M.; Shuai, J.; Zhang, H.; Yang, S.Q.; Zhang, Q.Y.; Ren, Z.F. Thermal conductivity reduction by isoelectronic elements V and Ta for partial substitution of Nb in half-Heusler $\text{Nb}_{(1-x)/2}\text{V}_{(1-x)/2}\text{Ta}_x\text{CoSb}$. *RSC Adv.* **2015**, *5*, 102469–102476. [[CrossRef](#)]
15. Zhu, T.J.; Fu, C.G.; Liu, X.H.; Liu, Y.T.; Zhao, X.B. High efficiency half-Heusler thermoelectric materials for energy harvesting. *Adv. Energy Mater.* **2015**, *5*, 1500588. [[CrossRef](#)]
16. Dow, H.S.; Kim, W.S.; Shin, W.H. Effect of C and N addition on thermoelectric properties of TiNiSn half-Heusler compounds. *Materials* **2018**, *11*, 262. [[CrossRef](#)] [[PubMed](#)]
17. Fu, C.G.; Zhu, T.J.; Liu, Y.T.; Xie, H.H.; Zhao, X.B. Band engineering of high performance p-type FeNbSb based half-Heusler thermoelectric materials for figure of merit $zT > 1$. *Energy Environ. Sci.* **2015**, *8*, 216–220. [[CrossRef](#)]
18. Fu, C.G.; Bai, S.Q.; Liu, Y.T.; Tang, Y.S.; Chen, L.D.; Zhao, X.B.; Zhu, T.J. Realizing high figure of merit in heavy-band p-type half-Heusler thermoelectric materials. *Nat. Commun.* **2015**, *6*, 1–7. [[CrossRef](#)] [[PubMed](#)]
19. Huang, L.H.; He, R.; Chen, S.; Zhang, H.; Dahal, K.; Zhou, H.Q.; Wang, H.; Zhang, Q.Y.; Ren, Z.F. A new n-type half-Heusler thermoelectric material NbCoSb. *Mater. Res. Bull.* **2015**, *70*, 773–778. [[CrossRef](#)]
20. Chai, Y.W.; Oniki, T.; Kimura, Y. Microstructure and thermoelectric properties of a $\text{ZrNi}_{1.1}\text{Sn}$ half-Heusler alloy. *Acta Mater.* **2015**, *85*, 290–300. [[CrossRef](#)]
21. Chai, Y.W.; Oniki, T.; Kenjo, T.; Kimura, Y. The effect of an isoelectronic Ti-Zr substitution on Heusler nanoprecipitation and the thermoelectric properties of a $(\text{Ti}_{0.2}\text{Zr}_{0.8})\text{Ni}_{1.1}\text{Sn}$ half-Heusler alloy. *J. Alloys Compd.* **2016**, *662*, 566–577. [[CrossRef](#)]
22. Pei, Y.Z.; Wang, H.; Snyder, G.J. Band engineering of thermoelectric materials. *Adv. Mater.* **2012**, *24*, 6125–6135. [[CrossRef](#)] [[PubMed](#)]
23. Liu, Z.H.; Wang, Y.M.; Mao, J.; Geng, H.Y.; Shuai, J.; Wang, Y.X.; He, R.; Cai, W.; Sui, J.H.; Ren, Z.F. Lithium doping to enhance thermoelectric performance of MgAgSb with weak electron–phonon coupling. *Adv. Energy Mater.* **2016**, *6*, 1502269. [[CrossRef](#)]
24. Liu, X.H.; Zhu, T.J.; Wang, H.; Hu, L.P.; Xie, H.H.; Jiang, G.Y.; Snyder, G.J.; Zhao, X.B. Low electron scattering potentials in high performance $\text{Mg}_2\text{Si}_{0.45}\text{Sn}_{0.55}$ based thermoelectric solid solutions with band convergence. *Adv. Energy Mater.* **2013**, *3*, 1238–1244. [[CrossRef](#)]
25. Pei, Y.Z.; Gibbs, Z.M.; Gloskovskii, A.; Balke, B.; Zeier, W.G. Optimum carrier concentration in n-type PbTe thermoelectrics. *Adv. Energy Mater.* **2014**, *4*, 1400486. [[CrossRef](#)]
26. Huang, L.H.; Zhang, Q.Y.; Wang, Y.M.; He, R.; Shuai, J.; Zhang, J.J.; Wang, C.; Ren, Z.F. The effect of Sn doping on thermoelectric performance of n-type half-Heusler NbCoSb. *Phys. Chem. Chem. Phys.* **2017**, *19*, 25683–25690. [[CrossRef](#)] [[PubMed](#)]
27. Zhao, H.Z.; Cao, B.L.; Li, S.M.; Liu, N.; Shen, J.W.; Li, S.; Jian, J.K.; Gu, L.; Pei, Y.Z.; Snyder, G.J.; et al. Engineering the thermoelectric transport in half-Heusler materials through a bottom-up nanostructure synthesis. *Adv. Energy Mater.* **2017**, *7*, 1700446. [[CrossRef](#)]
28. Ohno, S.; Aydemir, U.; Amsler, M.; Pöhls, J.H.; Chanakian, S.; Zevalkink, A.; White, M.A.; Bux, S.K.; Wolverton, C.; Snyder, G.J. Achieving $zT > 1$ in inexpensive zintl phase $\text{Ca}_9\text{Zn}_{4+x}\text{Sb}_9$ by phase boundary mapping. *Adv. Funct. Mater.* **2017**, *27*, 1606361. [[CrossRef](#)]

